

A low-cost, high-fidelity converging-beam Doppler instrument for measuring velocity and turbulence at tidal energy sites

Thomas Lake, David Glasby, Jose M. Horrillo-Caraballo, Michael Togneri, Ian Masters, Martin Austin and Ben Lincoln

Abstract—Traditional Acoustic Doppler Current Profiler (ADCP) instruments measure marine flow velocities along diverging acoustic beams. This allows estimation of approximate mean velocity and turbulence at a point between the beams. Alternatively, a converging beam instrument can measure velocity components at a single point and hence provide a higher quality measurement. Here we show a new design of instrument with converging beams together with some preliminary flow measurement results.

The instrument is constructed around a triangular frame with Doppler transceivers on the ends of cable stayed arms. It is designed to be installed and recovered from the seabed without use of a crane vessel. This is achieved by a pressurised air buoyancy system. The system can be slipway launched with a boat trailer and flat packed for transport on the same trailer. The system performed well for three test deployments; however, measurements of the seabed stability of the frame showed undesirable flexing of one arm when it was positioned perpendicular to the main flow direction.

A traditional ADCP was located on the frame and the two instruments were operated in burst mode, with each instrument measuring alternately every 20 minutes. Results for velocity and turbulent kinetic energy at the same depth are reported for both instruments and compared. A 2D oceanographic model of the deployment site is used as an additional point of comparison to illuminate some differences in the mean flow velocity observations of both instruments.

This instrument will add significantly to measurement capabilities at tidal stream turbine deployment locations. Improved turbulence measurements will give better understanding of turbine loading and hence improve reliability

Manuscript received 22 February 2023, accepted 18 December 2023, published 31 July 2024.

This is an open access article distributed under the terms of the Creative Commons Attribution 4.0 licence (CC BY <http://creativecommons.org/licenses/by/4.0/>). Unrestricted use (including commercial), distribution and reproduction is permitted provided that credit is given to the original author(s) of the work, including a URI or hyperlink to the work, this public license and a copyright notice. This article has been subject to single-blind peer review by a minimum of two reviewers.

This work was supported by the SELKIE project funded by the European Regional Development Fund through the Ireland Wales Cooperation programme; the WTIMITS project, funded by EPSRC via the Supergen ORE Hub Flexible Funding scheme, EP/S000747/1; and by the MEECE project funded by the European Regional Development Fund and the UK & Welsh governments through the Swansea Bay City Deal.

Thomas Lake, David Glasby, J-M. Horrillo-Caraballo, Michael Togneri and Ian Masters are at the Energy and Environment Research Group, Faculty of Science and Engineering, Swansea University Bay Campus, Swansea, SA1 8EN, UK

Martin Austin is at the School of Ocean Sciences, Bangor University, Menai Bridge, Anglesey, LL59 5AB, UK

Ben Lincoln is at the Smart Efficient Energy Centre, Centre for Applied Marine Sciences, School of Ocean Sciences, Bangor University, Menai Bridge, Anglesey, LL59 5AB, UK

Digital Object Identifier: <https://doi.org/10.36688/imej.7.11-24>

of these systems. The unit can also be used to deploy different types of sensors for oceanographic measurements.

Index Terms—Doppler instrument, tidal stream, marine turbulence

I. INTRODUCTION

It is notoriously difficult to perform maintenance operations on tidal stream turbines (TST) which has led the industry to consider carefully the long term reliability of turbines. Fluctuations in loading that lead to fatigue failure are related to transient flow features including turbulence and waves. It has been shown [1] that there is an almost linear relationship between turbulence strength and load variation. It is standard practice to deploy a diverging beam acoustic Doppler current profiler (ADCP) within potential tidal energy deployment sites, but this instrument requires compromises in the methods used to calculate turbulence statistics and also rendering it impossible obtain instantaneous estimates of mean velocity or turbulence. Velocity data measured with a ADCP can be analysed as ensembles of (typically) 5 to 15 minutes duration, and then statistical and spectral methods used to extract turbulent kinetic energy (TKE) density, integral lengthscales and other key parameters [2]. Both industrial and academic researchers [3], [4] have reviewed several of the important issues regarding turbulence measurement in the ocean, and have shown that existing ADCP units are not accurate enough for the most detailed engineering design required for tidal stream reliability. It has also been shown that there are limitations when using these diverging beam devices in flows with coherent turbulent structures[5].

In a laboratory environment, it is possible to measure turbulence with an acoustic Doppler velocimeter (ADV), which typically has three acoustic sensors focused on a measurement volume just outside the unit. The resulting data is of very high quality, but the very short distances from the unit to the measurement location make them less practical for field deployment. Therefore, there is now a body of work that attempts to develop a converging beam acoustic Doppler profiler (C-ADP). All proposed instruments of this type use a set of single beam acoustic Doppler profilers (S-ADP) which are positioned on a rigid frame at a set distance apart and focused inwards to a measurement volume in the same way as an ADV. In order to measure

turbulence at a useful distance from the sensor, the sensor separation is on the order of several metres.

An instrument of this type was installed at the European Marine Energy Centre, Orkney, UK in 2012 [6]. Sensors were installed on top of a tidal turbine, including four converging beams and a diverging beam AWAC. The sensor frame was 3.7m long and the focal point was 4m above the frame. Further work [7] extended this instrument to four movable beams and added two fixed S-ADP units. Results from the work show that C-ADP measured turbulence intensity is consistently lower than estimates from a standard ADCP. Harding et al.[8] report results from a four beam C-ADP with each beam actuated in two degrees of freedom so that the focal point of the measurement can be chosen by the user. Each beam is generated from a S-ADP. In this case, a frame of dimensions 4.9m x 2m was mounted vertically on a dock structure with the beams positioned at the corners. The beams were approximately horizontal, directed out into the channel from the dock. Samples were taken at 2Hz frequency. Validation of the results was achieved through an ADV instrument, floating on a tethered weight approximately 1m from the focal point.

Another approach to a converging-beam measurement of velocities has been tested in Nova Scotia with the Vectron platform developed by Hay et al [9]. The key difference between this instrument and the C-ADP tested at EMEC or the one described in the current study is its bistatic configuration i.e., the use of a single transmitter but multiple receivers. This approach requires careful synchronisation of the receivers with the transmitter, but eliminates the need to offset the measurement periods for the different receivers. Initial tests with a simplified geometry indicate that the Vectron is able to satisfactorily resolve the inertial subrange of turbulent velocities and achieve a substantially lower noise floor (by around two orders of magnitude) compared to typical broadband ADCPs.

Further alternative methods to improve on the turbulence measurements possible with ADCPs have been explored in recent studies: this includes the use of multiple linked ADCPs to allow estimation of all components of the Reynolds stresses [10], and adapting the five-hole pressure-transducer windspeed probe common in turbomachinery research for use in a marine environment [11]. Both of these alternatives offer significant improvements in turbulence sensing over conventional ADCPs, but have different goals from the converging beam target of a point measurement of velocity components at some distance from the instrument.

In this paper, we describe the design, testing and deployment of a new prototype instrument which aims to achieve the high-quality remote measurement of turbulence metrics typical of C-ADPs, but which is also designed to be compact and deployable without heavy

lifting vessels. We start in section II by discussing the design goals and process for the instrument, then in section III we give details of how the instrument was manufactured. Section IV gives details of the software used to regulate C-ADP data collection, and also the theoretical basis on which the collected data is used to calculate key flow properties. The pilot site, deployment and retrieval process are described in section V. The results obtained from the instrument are presented in section VI, supplemented by a comparison of the instrument data with a hydrodynamic model of the deployment site. Finally in section VII we discuss the results, draw the conclusions of the study and indicate some intended directions for further development of the instrument.

II. DESIGN OF THE INSTRUMENT

A. Design Goals

The goal of the instrument is to provide high quality robust measurements of turbulence metrics at a point corresponding to the typical hub height of bottom mounted MW scale tidal stream turbines. These units have 15-20m diameter rotors, so a measurement is needed at around 25m from the seabed. Beam angles of standard instruments are sufficient for measuring horizontal components of velocity, and so the instrument was designed to have a beam separation of approximately 10m. Given that such a large footprint is potentially difficult to deploy at sea and may require specialist vessels with a large deck area, the design goal also included the requirement for the unit to be flat packed for transit and with the potential to be self deploying. Desirable features established in the concept design stage included: use of the minimal number of sensors (three); use of a three legged structure to remove any rocking movement on the seabed; the ability for the unit to be towed to site and deployed safely; use of a compressed air driven buoyancy system for self recovery to the surface and tow to shore.

B. Physical structure

The primary purpose of the physical structure was to provide a rigid and lightweight frame on which the three S-ADPs can be mounted to form an equilateral triangle, with the ability to set the S-ADP beam angle and direction as required. It was important to ensure that the S-ADP were held steady throughout the deployment in order to produce high quality measurements. The frame was designed using off-the-shelf parts where possible to allow the design to be easily reproduced by anyone wishing to build their own C-ADP instrument. The frame was constructed from modular truss sections with conical connections that can be quickly assembled and disassembled by hand. The structural design consists of a central triangular frame with feet at each corner of the triangle, and an arm extending outwards from each corner of the triangle to create the desired distance between S-ADPs as shown in Figure 1. The horizontal stiffness of the arms was increased using wire ropes connected between the outside end of the arm and the central frame.



Fig. 1. Fully assembled frame on launch trailer, prior to buoyancy system test. ADP mounting points are shown at end of arms, but sensors are not installed in this image.

The target design weight has to be carefully chosen. A lower weight (in air) is desirable so that the unit can be assembled without use of lifting equipment and a lower wet weight reduces the required buoyancy volume. In contrast, the unit is gravity anchored and therefore a reasonable wet weight is required to maintain position on the seabed. All truss sections and fabricated frame parts were made from marine grade aluminium; this material was initially chosen over steel to achieve an overall wet weight of <400kg including the predicted weight of the sensor system and battery. At a later stage in the design process, the battery selection was changed to Li-ion type, significantly reducing the total weight, and consequently, ballast weights (scrap chain) were added to achieve the desired weight. The central triangle section of the frame provided an ideal space for mounting various pieces of equipment, including the data logger and battery housings, self-recovery system, 5-beam ADCP and battery pack, pressure transducers, secondary recovery system and ballast weight. The frame arms attach to the corners of the central triangle with the ability to pivot open and closed as illustrated in Figure 2, before being fixed in place. This allowed the fully assembled frame (equipment included) to be lifted and moved quickly and easily while working onshore; before and after the deployment. Having managed to keep the instrument as compact as planned, it is possible to launch and retrieve from a wider range of sites with more limited space; this includes the small boatyard from which the pilot deployment was carried out.

C. Subsystem design

a) Deployment System (raft and brake): - The C-ADP was deployed using a dedicated raft with slow release line; the C-ADP was secured underneath the raft, the raft was then towed by the work-boat to the test site where the C-ADP was manually lowered onto the seabed using a slow release line attached between the raft and the C-ADP. Once on the seabed the release line was retained, leaving the C-ADP with an unobstructed view of the water column above it. Figure 3 shows the raft and semi-submerged C-ADP during the tow operation.

b) Recovery System: - To recover the C-ADP from the seabed an automated air lift system was de-



Fig. 2. Frame with arms folded for storage and movement



Fig. 3. Deployment raft and C-ADP onsite at Warrior Way prior to seabed deployment



Fig. 4. Main image shows C-ADP post-deployment with primary recovery system clearly visible. The scuba tank is inside the frame on the left, with three barrels centre and right. Standard ADCP mounted in top of leg to left of image with its battery canister in blue just above the scuba tank. Inset panels show: (a) Primary recovery automated air release system during dry lab tests. Acoustic release on the left is attached to a weighted arm that opens an air pressure valve as it falls. This arm is visible in the open position in the main image. (b) Secondary recovery system mounted near centre of frame showing acoustic release and rope canister. Also visible are the batteries and battery mounting bracket.

signed which, when triggered using an acoustic release transponder, releases compressed air from a 12L scuba tank into three water filled 220L plastic barrels, adding sufficient buoyancy to lift the device off the seabed. Once resurfaced, the C-ADP was then towed back to shore. The recovery system is shown in Figure 4.



Fig. 5. Panel (a): ADP protective mounting bracket with manually adjustable pitch angle. Panel (b): C-ADP frame foot.

c) *Secondary Recovery System*: - A rope canister coupled with a secondary acoustic release transponder was mounted to the inner, more protected, section of the frame; when activated, this released a lifting line to the surface from which the whole frame could be hoisted by a winch onboard the work-boat. Although not required at any point, the secondary recovery system was triggered on two occasions to test its functionality and operated successfully in both cases. Panel (b) of Figure 4 shows the secondary recovery system mounted to the frame, post-deployment.

d) *ADP Housing*: - The ADPs were mounted inside a protective aluminium housing which fixes to an adaptor plate on the end of each of the frame arms, as shown in panel (a) of Figure 5. The housing and adaptor plate use a Vernier hole pattern to allow the ADP pitch angle to be set between 0 and 90 degrees with increments of 0.5 degrees.

e) *Anchoring System*: - The frame uses a combination of gravity and embedment type anchors; the triangular truss sections of the frame (above the feet) were used to hold ballast chain weight (total dry weight of 242kg across all three feet) while the plates on the underside of the feet embed into the seabed under the device's weight. The low centre of gravity created by the ballast weight helped to prevent the frame from tipping. The anchor-like feet proved sufficient to prevent the frame drifting on the seabed. Panel (b) of Figure 5 shows a foot with witness marks from embedment following the first deployment.

D. Staged development

The process of designing the instrument used a staged development method as recommended for ocean energy device development [12]. As a methodology, the stages were designed to increase performance while at lower TRL [13] reducing the overall time and risk in the project. As part of this process, it was decided to build a smaller scale but still functional unit prior to attempting to develop a unit of 10m from sensor to sensor. This interim stage unit was deployed at sea for a month to confirm the system viability. Overall, there were ten separate stages identified. Each of these provides risk reduction of later stages and proves various elements of the system. Table I shows the ten stages and the key learnings from each stage of the process. Many of the stages relate to the buoyancy system, which reaches TRL 6 by

then end of step 5 and TRL 7 with the full scale frame test at step 8. The sensor system was tested to TRL 4 in a laboratory water tank. Significant software interface issues were resolved at this stage, reducing risks of the full deployment. 24 hours at sea progressed the sensors to TRL 6 and the final test has delivered a complete system at TRL 7. Testing to date has been in the relatively calm waters of Milford Haven and further testing at a "commercial" tidal energy site is required before the system can be truly said to have reached the end of the development and TRL 9.

One valuable lesson from the smaller scale tests was the necessity to have good operating procedures while on shoreside; this improved the safety of the operations and ensured there were no delays in launching the system. Every operation to lower or raise the unit to the seabed was undertaken at slack water so keeping to time was essential for the testing.

The technical specifications of the full scale device are summarised in Table II, and represent the device as fitted for the full scale one-month deployment at the META Warrior Way test site between the end of January and end of February 2022.

III. MANUFACTURE AND DEPLOYMENT OF THE INSTRUMENT

A. Frame fabrication and assembly

a) *Fabrication*: - The frame was fabricated from aluminium and coated with marine grade aluminium paint by Metal Masters West Wales Ltd. The majority of the frame was made up from off-the-shelf stage truss components and fixings, with a number of bespoke fabricated components to create the frame corner pieces, feet and ADP mounts.

b) *Trial-build*: - An initial trial-build was performed at Swansea University Bay Campus in which all sub-systems were fitted to the frame, the ADP housings were aligned to the desired focal point in preparation for the Warrior Way deployment, and the deployment raft assembled and fitted over the top frame. The frame and raft were then flat-packed and transported to Rudders Boatyard near the test site, where the frame and sub-systems were re-assembled for deployment.

B. Electrical subsystem assembly

The ADPs were powered by two commercially available 140Ah Li-ion battery packs. These packs are designed for operation underwater and are housed in titanium pressure capsules, with all electrical connections made via waterproof connectors mounted on a removable bulkhead. One of the pressure capsules was custom manufactured to provide additional space for the control computer and associated electronics. Each ADP was provided with power and network connections made via bulkhead mounted connectors on this central electronics capsule. The two battery housings were then fitted to mounting brackets which clamped onto the frame central truss, with all external electrical and data connections made after the battery

TABLE I
A STAGED DEVELOPMENT PROCESS WAS USED TO REDUCE RISK WITH INCREMENTAL, COST EFFECTIVE STEPS. OPS. = OPERATIONS

Test Environment	Scale	Buoyancy system	Shoreside Ops.	Deployment Process	1 month durability	Recovery process	Data logging
1. Virtual (3D Solidworks)	Both	Y	Y	Y	Y	Y	
2. "Dry" lab	Both	Y			Y		
3. Dockside "dunk" test	2.5m	Y	Y				
4. Calm water 15 minute deployment	2.5m	Y	Y	Y		Y	
5. META Criterion Jetty 1 month deployment	2.5m	Y	Y	Y	Y	Y	
6. "Dry" system build and beam alignment	10m		Y				
7. Lab water tank test of sensors and data logging	10m		Y				Y
8. META Warrior Way 2 week deployment (no sensors)	10m	Y	Y	Y	Y	Y	
9. META Warrior Way 24h deployment	10m	Y	Y	Y		Y	Y
10. META Warrior Way 1 month full system	10m	Y	Y	Y	Y	Y	Y

TABLE II
DEVICE TECHNICAL SPECIFICATIONS

Technical Specification	Value/Properties
ADP-to-ADP horizontal distance	9.6m
ADP height above seabed	1.45m
Device wet weight	330kg
Device dry weight	505kg
Ballast weight (wet)	210kg
Primary Recovery System lift capacity	600kg (up to 40m depth)
Battery capacity	280Ah at 25V (nominal)
Data storage capacity	240GB
Duty Cycle	25% (15mins/hour) for 28 days

and electronics capsules were mechanically secured to the frame.

C. Deployment methodology

The deployment methodology was designed as a low cost operation, removing the need for a large vessel or a dive team. The chosen method, described in section II-C, was trialed initially on the 2.5m scale frame for the Criterion Jetty deployment (Table I stage 5), then a further three times on the 10m frame at the Warrior Way site. The raft frame (Figure 3) was constructed from scaffold pipes and clamps, and buoyancy provided by four 220L plastic barrels strapped to the four corners of the frame. A raised crossbar at the raft's bow was fitted with a number of cleats to tie off the slow release line described in section II-C and stabilising lines, allowing the crew to easily release the lines and allow the C-ADP to descend to the seabed when at the deployment location; this is shown in Figure 3. Three stabilising lines were used to secure the C-ADP to the underside of the raft during towing. The deployment line (or slow release line) passes through a friction brake attached to the raft; this added sufficient resistance to hold the C-ADP's wet weight so that the line could be

manually pulled by the crew for a safe and controlled descent to the seabed. The C-ADP was deployed with a weighted rope leading to a lump weight and marker buoy. The marker buoy, fitted with a GPS tracker, was used to monitor the C-ADPs location, both visually from shore, and remotely via the GPS tracker, during the three trial deployments at Warrior Way.

The whole deployment operation from the slipway launch up to returning to the boatyard lasted approximately 2 hrs. The operation was scheduled so that the deployment of the C-ADP and marker buoy at the test site were performed during slack water. This allowed the crew to drop the C-ADP as accurately and safely as possible at the chosen co-ordinates.

Pressure transducers were attached to each of the three feet. Depth measurements from these transducers during the Warrior Way deployments are shown in figure 10, and based on these measurements it is observed that the time to descend to the seabed on the slow release lines was approximately 5 minutes. Further analysis of the pressure transducer data throughout the duration of the deployment is given in section VI-A.

Recovery of the C-ADP operation was also performed during slack water. Once on site, the acoustic release transponder was triggered from the surface, initiating the air-lift recovery system as described in section II-C. Depth measurement data from the second and third Warrior Way deployments showed that the C-ADP took 30-35 minutes on average to become buoyant, after which the C-ADP rose to the surface in less than 1 minute. The marker buoy and ballast weight were then lifted using the workboat winch, and the C-ADP towed to the boatyard, as shown in Figure 6. A marker buoy may not be required in future deployments, meaning that this operation would be possible without any lifting capability. Once back at the boatyard, the frame was grounded on the slipway and the ADP arms folded in so it could be easily lifted up the slipway and disassembled.



Fig. 6. Recovery operation; return tow from Warrior Way to Rudders Boatyard

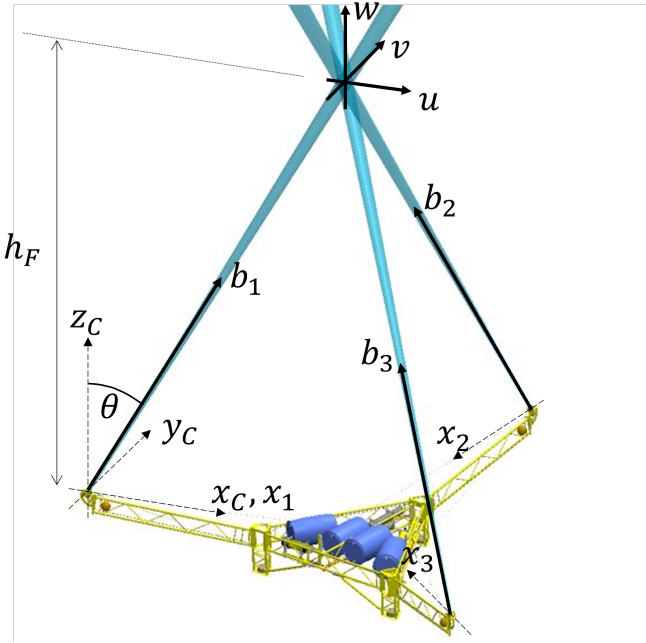


Fig. 7. Perspective view of the platform with beam and frame coordinates indicated. Cartesian velocity components measured at the focal point are also marked.

The secondary recovery system was triggered on the first and second deployments to test the system worked as intended. On both occasions the rope canister buoy had surfaced within 2 minutes of triggering the system. On the second occasion a larger buoy was used to improve its visibility from the work-boat deck.

IV. THEORETICAL PRINCIPLES

The basis on which the C-ADP operates is to combine approximately simultaneous measurements of along-beam velocities from the three single-beam ADPs, taken from a common sample volume (the “focal point”). This allows us to calculate instantaneous time series of all three velocity components for the flow passing through this volume. This is a simple geometric transformation - as can be seen in figure 7, it is straightforward to define the along-beam velocities

b_1, b_2, b_3 measured at the focal point in terms of the angle of the beams to the vertical, θ and the Cartesian velocities u, v, w at the same location as:

$$\begin{bmatrix} b_1 \\ b_2 \\ b_3 \end{bmatrix} = \begin{bmatrix} \sin \theta & 0 & \cos \theta \\ \cos \frac{2\pi}{3} \cdot \sin \theta & -\sin \frac{2\pi}{3} \cdot \sin \theta & \cos \theta \\ \cos \frac{2\pi}{3} \cdot \sin \theta & \sin \frac{2\pi}{3} \cdot \sin \theta & \cos \theta \end{bmatrix} \begin{bmatrix} u \\ v \\ w \end{bmatrix} \quad (1)$$

This equation is then inverted to obtain u, v, w from the recorded values of b_1, b_2, b_3 . The terms in $\frac{\pi}{3}$ arise due to the rotation of the x_2 and x_3 axes (i.e., the direction of the second and third beams projected into the horizontal plane) relative to the x_1 axis, which is arbitrarily selected to coincide with the ‘general’ C-ADP-relative axis x_C .

As described further in section IV-A, each single-beam ADP transmits with an offset of 83 ms relative to the other beams, in order to avoid detecting returns originating from another ADP’s transmitted pulse. Thus, for a given sample, beam 2 fires 83ms after beam 1, and beam 3 another 83ms after that. Strictly speaking, therefore, the sample time of each beam is slightly different. The times associated with the recorded data from each beam are based on the zero-offset time, i.e., the beam 1 firing time. The offsets are calculated with reference to the time taken for a ping to return to the transceivers from the surface at maximum expected depth, and this limited the sample rate to 4Hz, rather than the maximum 8Hz sampling frequency that the ADPs are capable of individually.

Calculating the u, v, w components of velocity by the inversion of equation 1 yields horizontal components u and v that are defined relative to the general C-ADCP axis x_C . To present the northerly and easterly horizontal velocity records in figure 14 in section VI-B, these are reoriented to north and east by a simple rotation based on the headings measured by the first C-ADP transceiver (i.e., the transceiver whose beam velocity is labelled b_1).

With time series of all three components of velocity at the focal point, it is straightforward to decompose the i th component into its time-average and fluctuating component as $u_i = \langle u_i \rangle + u'_i$, where angle brackets indicate an average over some suitable period and primed values indicate fluctuations about this average. From this decomposition the i, j th component of the constant-density Reynolds stress tensor can be simply calculated over the same averaging period as:

$$\tau'_{ij} = \langle u'_i u'_j \rangle \quad (2)$$

Of particular interest is the turbulent kinetic energy (TKE), k , which is half the trace of the Reynolds stress tensor:

$$k = \frac{1}{2} \langle u'_i u'_i \rangle, \quad (3)$$

using repeated index summation. Note that strictly speaking this is the per-unit-mass or specific TKE, but we refer to this simply as TKE for brevity.

A. Data collection and processing

To co-ordinate the operations of multiple individual ADPs, it was necessary to implement an onboard Ethernet network that allowed communication between the individual ADP units and a central control computer to provide timing, control, and data recording. A Raspberry Pi 4 computer provided the central control capability, with the addition of an external real time clock to allow accurate timing to be maintained in the absence of any off-frame source of information. These computers have been successfully used for data collection and control in previous projects [14]. This was then combined with software providing a Precision Time Protocol (PTP) service to allow the ADPs and control computer to synchronise their internal clocks and ensure consistent timestamping of recorded data, and more importantly allow for the firing of the individual beams to be offset to minimise interference between them as described above. This offset firing of connected units is a function provided by the firmware on the ADP units, but requires an external clock source to be provided. As the ADPs are required to be networked together to allow this synchronised operation, the opportunity was taken to stream data from each ADP throughout each deployment for separate recording on the control computer to provide some redundancy in case of equipment failure or damage.

The software used on the control computer was based on a Raspberry Pi OS minimal installation with a custom kernel to enable features required by ptp4l, which provided the PTP service. Control of the ADPs was provided by bespoke software written based on the information provided by Nortek in the Signature integrator's guide [15].

B. ADCP

To validate the measurements of mean velocity and turbulence obtained using the C-ADP, a Nortek Signature1000 ADCP was also deployed and mounted in the top of the corner of the central section of the frame within leg 1 (this is visible at the top of the front left leg in the main image of Figure 4). This position of the ADCP on the frame was chosen such that the focal point of the C-ADP lies within the sample volume of the ADCP for this deployment. An external battery housing was used and mounted on the frame (the smaller blue canister visible to the left of the main image in Figure 4). In order to ensure that the ADCP and C-ADP devices did not interfere with each other, the devices were configured to record at different times. The C-ADP device was configured to record at 4Hz for bursts of 5 minutes duration starting at 0, 20, and 40 minutes past each hour. The ADCP was then configured to record at 8Hz for bursts of 10 minutes duration starting at 7.5, 27.5, and 47.5 minutes past each hour. In early planning, the ADCP was to be oriented such that its x axis was parallel to one side of the frame and its y axis parallel with the

central truss section. However, this would lead to the beams of the ADCP intersecting with the beams of the C-ADP device in the event that the two instruments stopped operating on their scheduled timings, and so the ADCP was rotated an additional 22.5° clockwise as mitigation against this eventuality.

As with the C-ADP measurements of mean flow; northerly and easterly components of mean flow are calculated by simple rotation of the calculated instrument-relative mean flow components based on the heading measurement. To calculate the TKE values discussed in section VI-C, the standard variance method is employed as described in e.g., [16] and [17].

V. EXPERIMENTAL DETAILS

The Marine Energy Test Area (META) is a set of eight sites in and around Milford Haven in south west Wales, each pre-consented to allow the testing of marine energy devices and components[18]. These test sites are split into five quayside (or phase one) sites and three open water (or phase two) sites - including Warrior Way. The Warrior Way site is located on the south bank of the Daugleddau estuary, immediately south west of the Cleddau Bridge. The site covers 9.3 hectares with depths to 19m and with flow speeds advertised up to 1.2ms^{-1} [19]. Drop down video survey shows the seabed to be mainly small gravel.

Three test locations were used during the development of the C-ADP system, with initial "dunk" and calm water tests (Items 2 and 3 in Table I) conducted in Swansea Marina. The one month endurance test of the 2.5m device (Item 5 in Table I) was carried out at Criterion Jetty in Pembroke Dock - one of the phase one META sites. Principal testing of the full scale C-ADP device (Items 8–10 in Table I) was carried out at the META Warrior Way site, and the discussion and results presented below will focus on the results from the 3rd deployment at this site which took place between 29th January and 28th February 2022.

The C-ADP device was deployed on January 28th, reaching the seabed shortly before 14:30. The approximate location of the frame was 51.7036°N , 4.9267°W . The beam angles θ and the location of the focal point relative to the seabed h_F , as defined in Figure 7, are 45° and 9 m respectively. The C-ADP and ADCP were both configured to start automatically after 11:00 on January 28th to allow operation to be verified before deployment, with other settings as described above in Section IV.

VI. RESULTS

A. Frame Stability Assessment

As part of the trial deployments, self contained pressure loggers were deployed on the frame, as described in section III-C. The number of the beam attached to each arm will also be used to refer to the corresponding corner of the frame and pressure



Fig. 8. (L) Map of Wales showing computational model domain (shaded) and deployment area (outlined), with (R) detailed deployment area view showing C-ADP deployment location and the META Warrior Way site limits

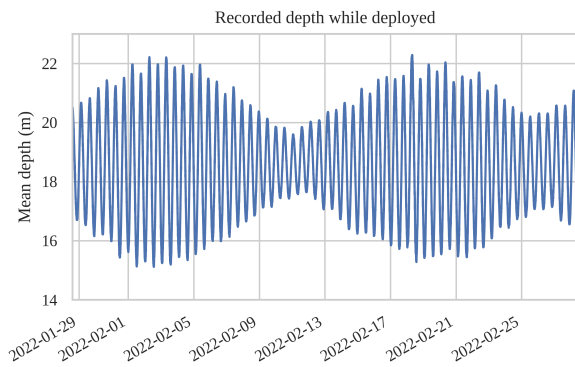


Fig. 9. Mean unit depth while deployed, as recorded by the three pressure sensors

sensor - i.e. beam 1 is mounted on the arm attached to corner 1, with the pressure transducer at the location referred to as PT1. The physical arrangement of the beams and their numbers is shown in Figure 7.

The recorded depths over the deployment are shown in Figure 9, confirming that the detected depth variation of 15-22m is consistent with the expected diurnal tide and spring-neap variations around an average depth of 18.6m. Note that the figure shows a mean across all sensors, as the differences between individual sensors are indistinguishably small in comparison to the changes in water depth.

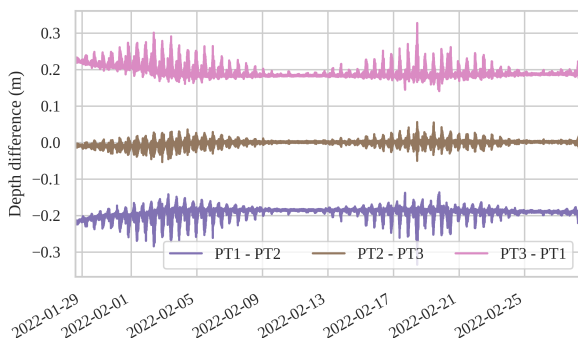


Fig. 10. Pairwise differences between depth recorded by the three pressure sensors

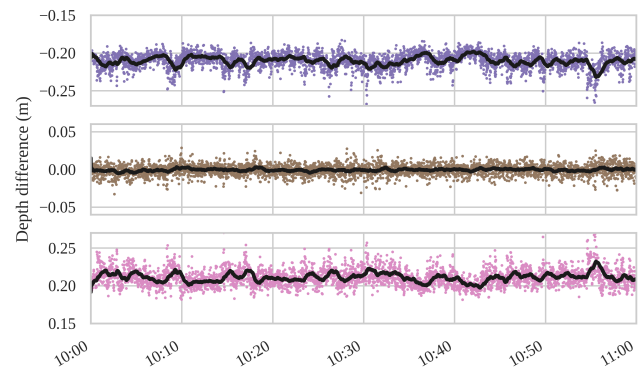


Fig. 11. Pairwise differences between depth recorded by the three pressure sensors on February 3rd. Black lines indicate a 1 minute rolling mean. Colours are the same as Figure 10

Differences between the sensors can instead be examined by taking the differences between each pair of sensor measurements. This allows us to examine the orientation and stability of the frame during the deployment, as visualised in Figure 10. It can be seen that there is an initial “settling” period over the first 5-6 days of the deployment, lasting until approximately 03/02/2022. In addition, there is a clear correlation between the magnitude of the variation in sensor-sensor depth difference and the spring-neap cycle visible in Figure 9.

The initial settling period shows a decrease in the magnitude of difference between both PT1 and PT2, and PT1 and PT3 over the first few days. The average differences over the first hour post deployment were -22cm (PT1-PT2), -1cm (PT2-PT3), and 22cm (PT3-PT1). This suggests that, over the first few days of the deployment, corner 3 sinks approximately 1cm relative to corner 2, and that corner 1 settles approximately 3cm relative to corners 2 and 3. In other words, the frame exhibits a slight tendency to level out over this initial period. Note that this method only considers the relative change between each corner, so any settling of the frame that affected all 3 corners uniformly (e.g., a gradual, uniform erosion of any sediment under all three feet) would not be distinguishable from these measurements.

Examining the longer-term differences, between the initial settling in period and the end of the deployment, there is a positive difference between PT3 and PT1, a negative difference between PT1 and PT2, and near zero difference between PT2 and PT3. This suggests that corner 1 sits at a shallower depth than corners 2 and 3. The average difference between PT1 and PT2, and between PT1 and PT3 is 19cm in both cases, with the average difference PT2 and PT3 being 0cm; this corresponds to a tilt angle for the central frame of approximately 3.5° from the vertical.

Looking in more detail at the increased variations seen during a spring tide, it can be seen that these peaks are largely small scale, high frequency variations

- generally less than 5cm from the long term mean, but with occasional peaks up to 10cm. This is illustrated in Figure 11, which shows a detailed view of the differences between PTs for a one-hour period on 03/02/22 (after the initial settling period and during a spring tide), split onto separate axes for ease of comparison. The black line on each plot shows a rolling one minute mean. We initially considered the possibility that the higher-magnitude variations in PT differences could be related to stronger wave breaking in spring tides due to the faster tidal current interacting with wind generated surface waves; however, an FFT of this data (not shown) reveals that this is broadband noise with no dominant frequencies. The most likely explanation is therefore that there is a small shift in the settled tilt angle of the frame on the bed as the current changes direction, and the magnitude of this shift is greater when the magnitude of tidal currents is greater i.e., during spring tides. The maximum change in tilt associated with these differences in depth at the PT locations is 1.8° .

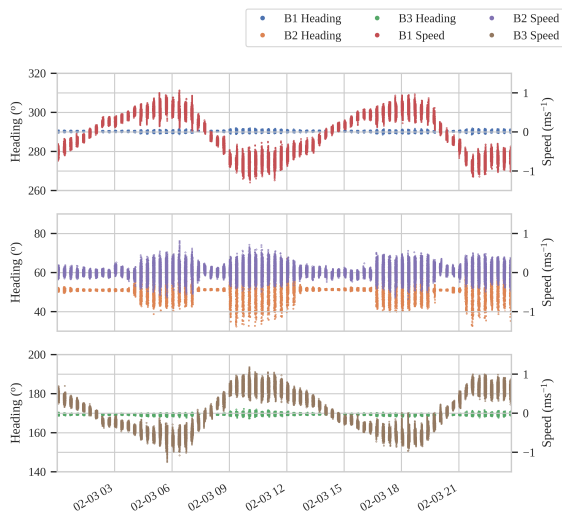


Fig. 12. Comparison of the heading and along beam flow speed at the focal point recorded by each beam over a spring tide

In addition to considering the stability of the instrument frame as a whole, the motion of each instrument can also be examined. Each sensor is equipped with a small magnetometer capable of providing heading, pitch, and roll information, which is recorded alongside the main beam data. As each sensor is mounted on its own arm, there is more scope for variation in the movement of the individual units.

In an initial examination of the heading data, all three sensors varied about a mean position that was consistent throughout the deployment; however, beam 2 exhibited much greater variation than beams 1 or 3. We hypothesise that this is due to the approximately perpendicular alignment of the arm supporting beam 2 with respect to the mean flow direction. This means that at times of stronger flow, periodic vortex shedding

may become established on the arm, causing it to oscillate around its attachment point to the frame and inducing the observed variation in momentum. This hypothesis is supported by the data visualised in Figure 12, which shows a single day's worth of beam velocity and heading data. It is clear from this that at times of low flow, the heading angle of beam 2 varies within an envelope of approximately $\pm 1^\circ$ around its mean value, similar to what is observed for beams 1 and 3. However, when the flow is faster, the envelope of heading variation for beam 2 becomes much greater (approximately $\pm 10^\circ$); this is also associated with greater variability in the velocity measured by beam 2. Moreover, the transition from the low-amplitude to high-amplitude heading oscillations is very abrupt, which suggests that it is associated with a qualitative change in flow regime, such as the establishment of von Kármán shedding.

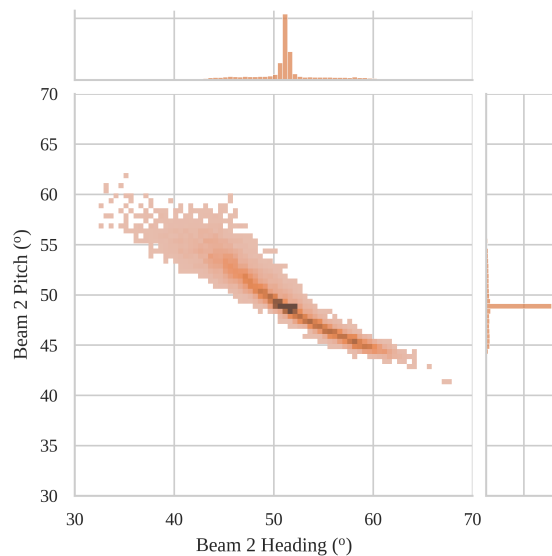


Fig. 13. Histogram showing correlation between heading and pitch recorded by the beam 2 sensor during a spring tide

This conclusion is reinforced by the data in Figure 13, which shows a two-dimensional histogram of heading and pitch for beam 2 during the same period, with darker colours representing higher counts. This reveals a clear correlation between pitch and heading, although the vast majority of the population is narrowly distributed around the central values. This is consistent with generally low amplitude variations and occasional large-magnitude excursions, and the shape of the distribution also indicates that the variation in heading and pitch are coupled - i.e., it suggests that the increased variation in heading for beam 2 is due to genuine motion of the supporting arm and not a sensor fault.

B. Mean flow

Figure 14 shows the comparison of the East and North velocities from the ADCP and the C-ADP at the focal point. The two instruments in general agree well. The two velocity components exhibit a clear

semi-diurnal variation, shifting between a northwest-flowing flood and a southeast-flowing ebb, as expected from the channel alignment shown in the right-hand panel of figure 8. There is very close agreement between the C-ADP and the ADCP over the whole data set for both components.

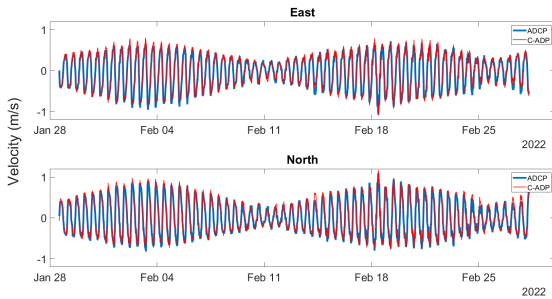


Fig. 14. Burst Averaged East (top panel) and North (bottom panel) velocities from C-ADP and ADCP at the focal point

In figure 15, the mean velocity components from the two devices are compared using a scatter plot. Visualising the results in this way shows the goodness of fit in both easterly and northerly velocity components. The C-ADP reproduces quite well the East and North velocity components with correlation coefficients R of 0.976 and 0.986 respectively.

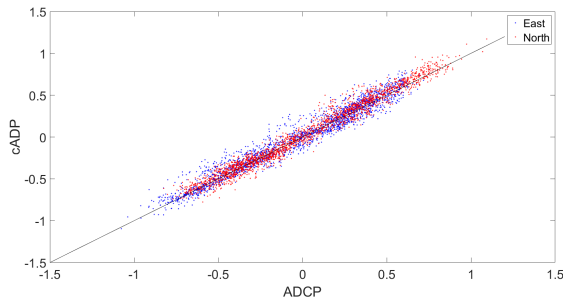


Fig. 15. Burst averaged East (blue) and North (red) velocities from C-ADP and ADCP at the focal point

C. Turbulence

The TKE for the C-ADP was calculated using Equation 3 and for the ADCP using the variance method as described at the end of section IV-B; here, we present a comparison of the TKE values averaged over each burst for the whole deployment dataset. Note that since the ADCP samples for longer than the C-ADP does (10 rather than 5 minutes) and at a higher frequency (8 rather than 4 Hz), its estimates of TKE are obtained using a significantly larger number of samples and we would therefore expect these to exhibit a lower sample variance than the C-ADP even if both instruments were measuring exactly the same flow. To make these comparisons more meaningful, therefore, the ADCP estimates of TKE shown in figures 16 to 18 are calculated for each burst using only half the burst duration and downsampled to 4 Hz.

Figure 16 shows an overview of the TKE comparison. Generally, during spring tides, C-ADP estimates

of TKE are greater than estimates of TKE obtained from the ADCP. However, during neap tides, values of C-ADP and ADCP TKEs shows similar values. This pattern is repeated at shorter timescales, as seen in the comparison of the TKE estimates from the two instruments over a single tidal cycle during peak spring tides shown in Figure 17. While close agreement is shown during slack water (i.e., when TKE values are low), the C-ADP estimates higher peak values of TKE during peak flow times. In addition, the C-ADP also estimates a less smooth TKE peak; there are multiple sharp peaks in TKE during most floods and ebbs, compared to the relatively smooth and broad increase and decrease over each tidal phase seen in the ADCP data.

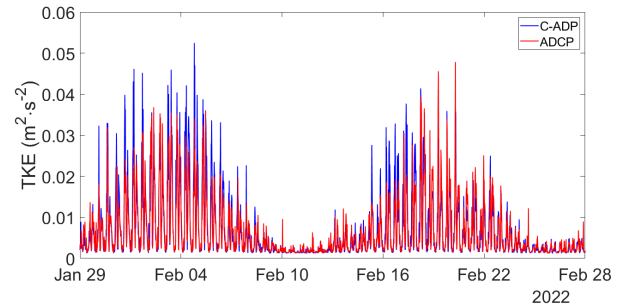


Fig. 16. Burst averaged TKE from the C-ADP and ADCP

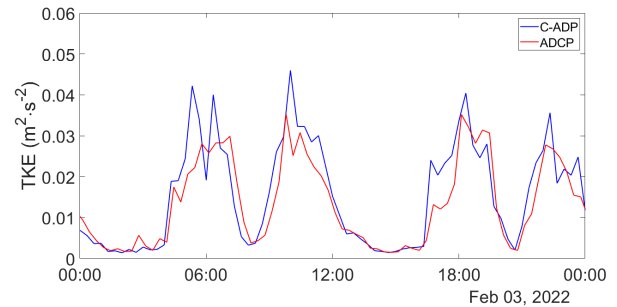


Fig. 17. Burst averaged TKE from the C-ADP and ADCP over a tidal cycle

In figure 18, a Q-Q plot is used to examine at what TKE values the two instruments' estimates start to diverge. This shows that values of TKE below $0.15\text{m}^2 \cdot \text{s}^{-2}$ compare well between the two instruments, but above this the C-ADP strongly tends to estimate higher TKE for the ADCP.

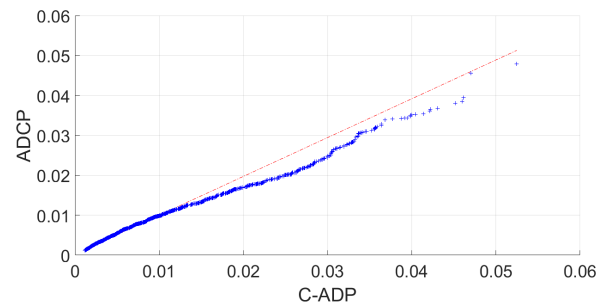


Fig. 18. Q-Q plot of burst-average TKE values from C-ADP and ADCP

D. Comparison with depth averaged model

In addition to comparing the measurements of the two instruments with one another, we have also investigated how both datasets compare with a hydrodynamic model of the estuary. The motivation for this comparison is threefold: first, to catch any systematic errors that might affect the performance of both instruments; second, to use the model to help identify C-ADP measurements that might be affected by the motion of the frame (cf. Subsection VI-A); and thirdly, to cross-validate the results of the model itself, which was not possible when the original modelling exercise was carried out [20].

The numerical model used for the comparison in this study is the DELFT3D package developed by WL-Delft Hydraulics in close cooperation with Delft University of Technology. Its design case is simulation of flows in coastal areas, shallow seas, estuaries, lagoons, etc., and the number of hydrodynamic processes included in the module DELFT3D-FLOW has broadened the number of problems to which it is applicable [21]. Its 2DH version (depth-averaged) solves the unsteady shallow-water equations in one-layer (vertically homogeneous) fluids and has been applied in many studies around the world [22].

The specific model used in this study covers the Milford Haven estuary and waterways, and is hereafter referred to as MHW. The northern boundary is located between Haverfordwest (Western Cleddau) and Blackpool Bridge (Eastern Cleddau). The western boundary is located over the $5^{\circ}12'W$ longitude line between Hooper's Point and the point ($51^{\circ}36'45''N$, $5^{\circ}12'W$), and the southern boundary lies between the point ($51^{\circ}36'45''N$, $5^{\circ}12'W$) and a point near Linney Head; the extent of the domain is shown in the left-hand panel of figure 8. The grid contains 1294×632 cells, and grid spacing is approximately $20 \times 30m$. Boundary conditions were specified by imposing amplitudes and phases of pre-selected tidal constituents (M2, S2, N2, K2, K1, O1, P1, Q1, MF, MM, M4, MS4 and MN4) at the nodes of the open boundaries. The model calibration and validation is described in greater depth in Horrillo-Caraballo *et al.* [20].

Figure 19 shows the comparison between the velocity magnitudes (in panel (a)) and headings (in panel (b)) of the C-ADP, ADCP and the model MHW. Horrillo-Caraballo *et al.*[20] found during their study that the velocities reported by the model are lower than the velocity magnitudes obtained by earlier ADCP measurements, and that the model seems to perform better during spring tides than during neap tides. In the current study, the MHW model overestimates the low velocities compared to C-ADP observations, but similar to the previous comparison it exhibits better agreement during the spring tides than neap tides. A similar pattern is also borne out when comparing the model results with the ADCP data.

Scatter plots of velocity magnitudes of the C-ADP and ADCP observations compared to the MHW predictions are shown in panels (a) and (b) of figure 20; points in the scatter are colour-coded according to the

heading from the instruments. From these figures, it appears that the ADCP-MHW data is dispersed more widely around unity than the C-ADP-MHW data; linear fits of the scatter confirm this, giving R^2 values of 0.744 for the C-ADP-MHW comparison and 0.641 for the ADCP-MHW comparison. The C-ADP data is also better correlated with the MHW observations (R 0.863 vs. 0.801).

Figures 20c and 20d show that the model predicts the same mean direction of flow for both ebb and flood as is detected by the instruments, but significantly underestimates the variability around this mean heading. In panels (c) and (d) of figure 20, it is clear that most times agree well between the instruments and the model, with the vast majority of points clustering in the top right (flood) or bottom left (ebb). The values that appear in the top left and bottom right are due to the model predicting the change in direction of the low-magnitude velocities at slack tide on average 18 minutes earlier than is observed with the instruments. These points account for 10.8% of the data shown in panel (c) and 8.3% of the data in panel (d).

VII. DISCUSSION AND CONCLUSIONS

A. Design Review

This paper has considered two aspects of converging beam acoustic measurements: firstly the practical elements of a physically large instrument, and secondly a consideration of the data that can be provided by this instrument. The design process was based on key design goals and a risk minimisation process. The design criteria of portable, hand assembly and minimal lifting equipment requirements were all met to some level, while the incremental stage gate process did succeed in significantly reducing risk so that when the later field work stages took place the operations went reasonably smoothly.

The system is portable and can be transported using a van and small boat trailer. This was facilitated by the use of off-the-shelf sections, but some of the connection systems were more complex than needed. On reflection, there could have been more rationalisation in the connectors and a slightly lower part count. The main disadvantage of the portable design was the flexibility of the arms as discussed in the data above, resulting in oscillation. We hypothesise that this may be due to the vortex shedding from the arm. Future deployments will therefore use an updated design of the arm that utilising stiffer triangular beams.

The whole unit was hand assembled and this was possible with a team of four in a few hours prior to a deployment. Recovery, disassembly, demobilisation and return to the lab took less than a day with a team of five.

Removal of lifting operations was partially achieved. We showed that although it was possible to trailer launch the unit, use of a telehandler made the launch significantly quicker and easier. All the operations at sea related to the unit did not require specialist equipment or lifting gear so this design goal was met very successfully. On one occasion, a replacement

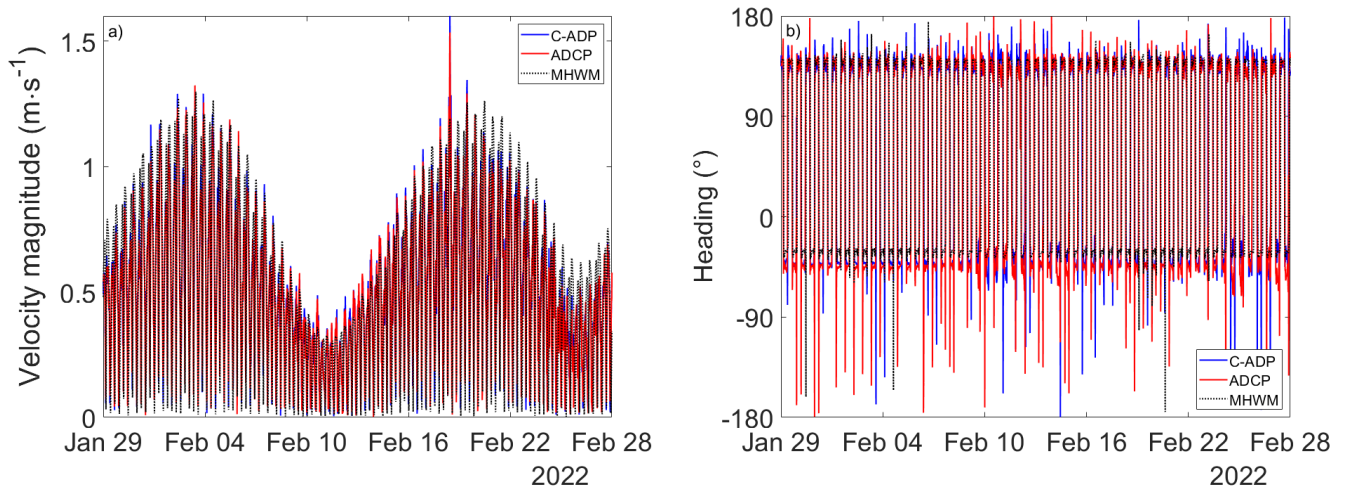


Fig. 19. Comparison of velocities and headings between C-ADP, ADCP and model. (a) Velocity magnitudes and (b) Headings

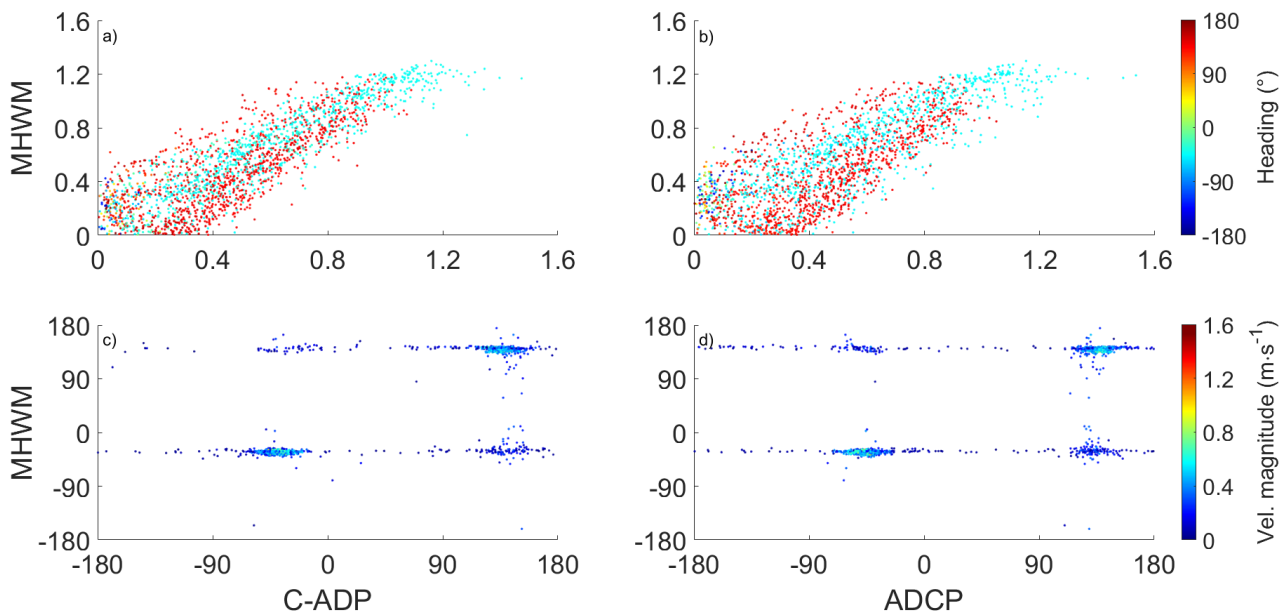


Fig. 20. Scatter plots of: (a) C-ADP and MHW velocity magnitudes with colour-coded headings, (b) ADCP and MHW velocity magnitudes with colour-coded headings, (c) C-ADP and MHW headings with colour-coded velocity magnitudes and (d) ADCP and MHW headings with colour-coded velocity magnitudes.

vessel was used at short notice, proving the flexibility of the deployment and retrieval procedure. The only exception was the navigational safety marker buoy that used a standard mooring and this was recovered using a deck winch.

The success of the automated recovery system and the flexibility of the frame will allow the design to be utilised for other sensor systems. The buoyancy can be adjusted quite easily and allows a significant payload. In the marine energy context, this could be used for active sonar (fish tracking), sediment and nutrient monitoring. The distance between the arms provides a fixed distance between synchronised instruments and this could be useful for acoustic measurements of marine mammals.

B. Experimental conclusions

The C-ADP and ADCP estimates of mean velocity agree very well, indicating that the novel instrument can at least match the current state of the art for measuring mean tidal currents. Perhaps more importantly, the C-ADP measurements of mean flow agree better with model results for the deployment site. This indicates that despite the possible issues with the unsteady beam, the C-ADP's use of three sources of data for the same location yields a better estimate of mean flow properties than the conventional diverging-beam ADCP, as an additional advantage on top of its capacity to measure high-frequency multi-component velocity data at the focal point.

The two instruments' estimates of TKE agree well for values up to approximately $0.15\text{m}^2 \cdot \text{s}^{-2}$, but at higher turbulence the C-ADP estimates consistently

greater values than the ADCP. Since the key difference between the C-ADP and ADCP estimation methods is the assumption of spatial homogeneity that is required to derive a single TKE value from the four diverging beams of the ADCP, this suggests that the implicit spatial averaging causes ADCP estimates of TKE to be biased low. This could potentially be due to the beam separation at the height of the focal point effectively acting as a low-pass wavenumber filter, excluding turbulent features of smaller size from the calculated TKE. As the turbulence becomes more energetic at higher speeds and the energy-bearing subrange of the spectrum extends to higher wavenumbers, this could mean that part of the significant turbulent energy goes undetected by an ADCP using the variance method, explaining the gap between the instruments at high TKE values.

Alternatively, the higher estimated TKE values from the C-ADP could be associated with the apparent motion of the arm on which beam 2 is mounted, as discussed at the end of section VI-A. As noted above, during the deployment of the C-ADP, the heading of beam 2 was very closely aligned with the cross-stream direction (i.e., the v -component of velocity). The oscillations in heading of this beam at times of high flow mean that the measured values will have recorded a greater proportion of the along-stream u -component than would have been the case if the frame had been perfectly rigid. Since the along-stream velocity is greater than the cross-stream velocity, this will introduce a positive bias to the estimate of $\langle v'^2 \rangle$, and in turn will also bias the estimate of TKE high. Finally, it is possible that both these mechanisms are significant contributors to the overall difference in the TKE values estimated from the two instruments.

C. Future work

The C-ADP measurements reported in this paper pertain only to observations from the focal point. However, it is also possible to record data simultaneously at other bins throughout the water column; in effect, the C-ADP can act as a 3-beam ADCP at depths other than the focal depth. In future deployments, it will be possible to analyse this data from other vertical locations to see if any trends emerge related to the physical distance between the measurement points. The principal difficulty to be expected with this will be the problem of disentangling effects of beam separation from genuine vertical variation in mean flow or TKE; however, retaining the simultaneous deployment of the ADCP will be useful in the portion of the water column below the focal point, where it will be possible to compare measurements of the same underlying vertical variation as measured by two instruments whose beam separation behaves differently (increasing with height for the ADCP, decreasing for the C-ADP).

The data analysis will also be extended to consider spectral properties of turbulence. The C-ADP's capacity to capture high-frequency time series of multiple components of velocity at the focal point will make it possible, in particular, to test the assumption of

anisotropy in the inertial subrange of the velocity spectrum. This assumption is an important part of the model of a universal turbulent spectrum that predicts the characteristic $-5/3$ slope of the Kolmogorov cascade, and therefore underpins spectral-fitting estimates of turbulent dissipation. It has been possible to use this method with individual ADCP beams (see for instance [23]), but this of course is limited to estimation using a single component of velocity aligned with the direction of the beam used. With the three-component measurements enabled by the C-ADP, it will be possible to confirm whether this method yields similar estimates of dissipation regardless of the velocity component used and, if not, to investigate the extent to which turbulent isotropy remains significant at the scales on which Doppler measurement is possible.

VIII. ACKNOWLEDGMENT

The authors thank Ben Powell of the School of Ocean Sciences at Bangor University for his assistance and advice during the full scale deployments.

REFERENCES

- [1] M. Togneri, G. Pinon, C. Carlier, C. C. Bex, I. Masters, Comparison of synthetic turbulence approaches for blade element momentum theory prediction of tidal turbine performance and loads, *Renewable Energy* 145 (2020) 408–418.
- [2] M. Togneri, I. Masters, Micrositing variability and mean flow scaling for marine turbulence in Ramsey Sound, *Journal of Ocean Engineering and Marine Energy* 2 (1) (2016) 35–46.
- [3] N. S. Draycott, B. Sellar, T. Davey, D. Noble, V. Venugopal, D. Ingram, Capture and simulation of the ocean environment for offshore renewable energy, *Renewable and Sustainable Energy Reviews* 104 (2019) 15–29.
- [4] K. Black, J. Ibrahim, R. Hellsby, J. McKay, T. Clark, N. Pearson, R. Moore, J. Hernon, Turbulence: Best practices for measurement of tidal flows. A guide for the tidal power industry., Tech. rep., Partrac; Ocean Array Systems; ABPmer; ITP (2015).
- [5] N. S. Lucas, M. J. Austin, T. P. Rippeth, B. Powell, P. Wakonigg, Turbulence and coherent structure characterisation in a tidally energetic channel, *Renewable Energy* 194 (2022) 259–272. doi:10.1016/j.renene.2022.05.044.
- [6] B. Sellar, S. Harding, M. Richmond, High-resolution velocimetry in energetic tidal currents using a convergent-beam acoustic Doppler profiler, *Measurement Science and Technology* 26 (8) (2015) 085801.
- [7] B. G. Sellar, G. Wakelam, D. R. Sutherland, D. M. Ingram, V. Venugopal, Characterisation of tidal flows at the European Marine Energy Centre in the absence of ocean waves, *Energies* 11 (1) (2018) 176.
- [8] S. Harding, M. Dorward, B. Sellar, M. Richmond, Field validation of an actuated convergent-beam acoustic Doppler profiler for high resolution flow mapping, *Measurement Science and Technology* 32 (4) (2021) 045904.
- [9] A. E. Hay, L. Zedel, S. Nylund, R. Craig, J. Culina, The Vectron: A pulse coherent Doppler system for remote turbulence resolving velocity measurements, in: 2015 IEEE/OES Eleventh Current, Waves and Turbulence Measurement (CWTM), IEEE, 2015, pp. 1–2.
- [10] M. Thiébaud, J.-F. Filipot, C. Maisondieu, G. Damblans, R. Duarte, E. Droniou, S. Guillou, Assessing the turbulent kinetic energy budget in an energetic tidal flow from measurements of coupled ADCPs, *Philosophical Transactions of the Royal Society A* 378 (2178) (2020) 20190496.
- [11] A. M. Young, N. R. Atkins, C. J. Clark, G. Germain, An unsteady pressure probe for the measurement of flow unsteadiness in tidal channels, *IEEE Journal of Oceanic Engineering* 45 (4) (2019) 1411–1426.
- [12] N. Mendoza, T. Mathai, D. Forbush, B. Boren, J. Weber, J. Roberts, C. Chartrand, L. Fingersh, B. Gunawan, W. Peplinski, et al., Developing technology performance level assessments for early-stage wave energy converter technologies, Tech. rep., National Renewable Energy Lab.(NREL), Golden, CO (United States) (2021).

- [13] J. Weber, WEC Technology Readiness and Performance Matrix - finding the best research technology development trajectory, in: Proceedings of the 4th International Conference on Ocean Energy, Dublin, Ireland, Vol. 17, 2012, pp. 1–10.
- [14] T. Lake, J. Hughes, M. Togneri, A. J. Williams, P. Jeffcoate, R. Starzmann, N. Kaufmann, I. Masters, Strain gauge measurements on a full scale tidal turbine blade, *Renewable Energy* 170 (2021) 985–996. doi:10.1016/j.renene.2021.01.137.
- [15] Nortek AS, Nortek Manuals. Signature Integration, Tech. rep. (2017).
- [16] Y. Lu, R. G. Lueck, Using a broadband ADCP in a tidal channel. Part II: Turbulence, *Journal of Atmospheric and Oceanic Technology* 16 (11) (1999) 1568–1579.
- [17] M. T. Stacey, S. G. Monismith, J. R. Burau, Measurements of Reynolds stress profiles in unstratified tidal flow, *Journal of Geophysical Research: Oceans* 104 (C5) (1999) 10933–10949.
- [18] About META - META Wales, <https://www.meta.wales/about-meta/>, accessed 2022-06-27 (12 2021).
- [19] Warrior Way - META Wales, <https://www.meta.wales/facilities/phase-2-sites/warrior-way/>, accessed: 2022-06-27 (09 2019).
- [20] J. M. Horrillo-Caraballo, I. Fairley, H. U. Karunarathna, I. Masters, D. E. Reeve, Investigation of the tidal resources in the area of Milford Haven. technical report of the seacams2 project (sc2-r&d-s35) with Marine Energy Wales, Tech. rep., Swansea University, Swansea, Wales (United Kingdom) (2021).
- [21] G. Lesser, J. Roelvink, J. van Kester, G. Stelling, Development and validation of a three-dimensional morphological model, *Coastal Engineering* 51 (2004) 883–915. doi:10.1016/j.coastaleng.2004.07.014.
- [22] DELTARES, Delft3D-FLOW Simulation of multi-dimensional hydrodynamic flows and transport phenomena, including sediments. Hydro-Morphodynamics. User Manual. version 3.15.34158, Tech. rep., DELTARES, Delft (The Netherlands) (2014).
- [23] M. Guerra, J. Thomson, Turbulence measurements from five-beam acoustic Doppler current profilers, *Journal of Atmospheric and Oceanic Technology* 34 (6) (2017) 1267–1284.